

Incorporating Tube-to-Tube Clearances in the Kinematics of Concentric Tube Robots

Junhyoung Ha and Pierre E. Dupont, *Fellow, IEEE*

Abstract—Mechanics-based formulations of concentric tube robots incorporate tube bending and twisting, but do not include other phenomena that could model observed hysteretic behavior in which tube configurations reached by rotating tubes in different directions achieve different tip positions. As a step toward incorporating hysteretic tube-on-tube friction, this paper derives a model that enables computation of the contact forces applied by the tubes on each other along their lengths. To do so, it is necessary to include the small, but finite clearances between the tubes. Recasting the constrained energy minimization problem as its dual problem enables numerically efficient solution for the clearance-constrained centerlines of each tube as well as their contact forces. These variables are investigated through numerical examples and it is shown that, even without considering friction, the assumption of zero clearance can introduce tip position errors of several millimeters for clinically relevant robot lengths.

I. INTRODUCTION

Concentric tube robots have found application for many types of surgery including inside the heart [1]–[4], the brain [5], [6] and the lungs [7]–[9]. Many of these implementations have employed a mechanics-based kinematic model derived from the Cosserat rod model [10], [11] or a potential energy formulation [12], [13]. While the resulting kinematic model is more complex than standard robot models, real-time implementations have been successfully demonstrated [5]. The model is approximate, however. For example, the mean and the maximum modeling errors in the tip position predictions are 4.2/8.3mm for 207mm long robot [10] and 2.89/8.49mm for around 200mm long robot [11]. Since targeting errors of 1-2mm can be significant in surgeries performed near critical structures, this is a significant level of modeling error, which currently must be compensated for, often using imaging feedback.

Furthermore, the current model does not provide the capability to include observed hysteretic behavior such as shown in Figure 1. Two unmodeled phenomena that could be responsible for this behavior are friction between the tubes and nonlinear hysteretic elasticity. While the relative contribution of these phenomena is not well understood, the influence of lubricants on the effect shown in Figure 1 has been observed by the authors. To investigate how much of the unmodeled behavior may be due to friction, this paper takes the first steps toward formulating a mechanics-based model of tube-on-tube friction by deriving expressions for the distributed contact forces between the tubes.

*This work was supported by the NIH under grant R01HL124020.

Junhyoung Ha and Pierre E. Dupont are with the Department of Cardiovascular Surgery, Boston Children's Hospital, Harvard Medical School, Boston, Massachusetts, USA.

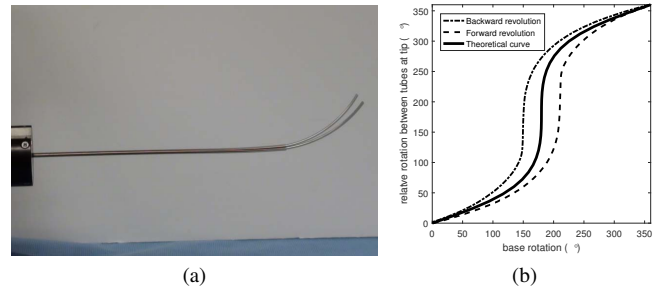


Fig. 1. Examples of hysteresis: (a) superimposed semitransparent robot shapes of same configuration with clockwise and counterclockwise base rotations, (b) base rotation versus relative rotation between a pair of tubes at tip.

This is challenging since the current model assumes that all overlapping tubes conform to a single centerline curve, which implies that there is no clearance between tubes. In reality, however, a finite clearance must be used, i.e., a small gap must exist between the outer diameter of the inner tube and inner diameter of the outer tube. If this clearance is too small, the tubes bind up and cannot be rotated and translated. It is necessary to include clearance in the model in order to compute the distribution and magnitude of the inter-tube contact forces. While it is clear that friction depends on the contact force distribution between tubes, the inclusion of clearance also addresses a secondary modeling error. When a tube extends beyond the end of another tube, a zero-clearance model predicts that the longer tube extends along the tangent at the tip of the shorter tube. The introduction of clearance, however, can correctly predict the misalignment between the two centerline tangent vectors at the tip of the shorter tube.

The contribution of this paper is to derive a convex-optimization-based kinematic model that solves for inter-tube contact forces as a function of inter-tube clearance. The formulation minimizes elastic potential energy while allowing each tube's centerline curve to vary within the clearances of its inner and outer neighbors. Numerical experiments are presented to show the effect of clearance on robot shape, tip position prediction, and contact force distribution.

The paper is organized as follows. The kinematics in the presence of tube clearances are derived in Section II as an optimization problem. Section III presents a set of numerical experiments to investigate the effect of the clearance on the robot shape and the contact force distribution between tubes. Finally, a conclusion is presented in Section IV.

II. KINEMATICS IN PRESENCE OF TUBE CLEARANCE

Consider a concentric tube robot with n tubes. The robot is parameterized with an arc-length parameter s along the length. The tubes are numbered increasingly from the outermost one (tube 1) to the innermost one (tube n). Tube i has its own pre-curvature function $\hat{u}_i(s) \in \mathbb{R}^{3 \times 3}$ and bending and torsional stiffness $k_{i,xy}, k_{i,z} \in \mathbb{R}$.

The mechanics-based kinematics provides an elastic equilibrium of the tubes. The kinematics can be mathematically summarized as a map from base rotations and translations to the bending curvatures and torsional curvatures (twist rates) of the tubes [10], [11]:

- input: (θ_b, l_b)
- output: $u_i^*(s)$ for $s \in [l_{i,b}, L_i]$ and $i = 1, \dots, n$

where $\theta_b = [\theta_{1,b}, \theta_{2,b}, \dots]^T \in \mathbb{R}^n$ and $l_b = [l_{1,b}, l_{2,b}, \dots]^T \in \mathbb{R}^n$ are the base rotations and translations of the tubes, respectively, and $u_i^*(s) \in \mathbb{R}^3$ is the three dimensional curvature function of tube i at the elastic equilibrium whose x - and y -components are the bending curvature and z -component is the torsional curvature and $s = L_i$ is the distal end of tube i . The body frames and the centerline curves of the tubes, $R_i(s)$ and $p_i(s)$, are then computed from $u_i^*(s)$ by

$$\begin{aligned} \dot{R}_i(s) &= R_i(s) [u_i^*(s)] \\ \dot{p}_i(s) &= R_i(s) \hat{e}_z \end{aligned} \quad (1)$$

with the boundary conditions

$$\begin{aligned} R_i(l_{i,b}) &= R_z(\theta_{i,b}) \\ p_i(l_{i,b}) &= [0 \ 0 \ l_{i,b}]^T \end{aligned} \quad (2)$$

where $\hat{e}_z = [0 \ 0 \ 1]^T$ and the upper dot represents the derivative w.r.t. s . Note that $[\cdot]$ is the 3×3 skew symmetric matrix representation of 3-dimensional vector and $R_z(\theta) \in \mathbb{R}^{3 \times 3}$ is the rotation matrix of the frame rotated by θ about z -axis from $I_{3 \times 3}$. The solution of the kinematics satisfies $p_i(s) = p_j(s)$ for any tube i and tube j since this is one of the simplifying assumptions of the kinematics.

The computation of $u_i^*(s)$ involves solving a set of differential equations, the details of which can be found in [10], [11].

A. Kinematics in presence of clearance

Prior modeling work has assumed that all tubes share an identical centerline [10]–[13]. When there are clearances between tubes, however, the centerlines can differ from tube to tube within the clearances. Following the potential energy formulations in [12], [13] and relaxing the assumption of shared centerline, the mechanics of the tubes in the presence of nonzero clearance can be expressed as the following infinite dimensional optimization:

$$\min_{\{u_i(s)\}_{i=1, \dots, n}} \sum_{i=1}^n \int_{l_{i,b}}^{L_i} g_i(s) ds \quad (3)$$

where

$$g_i(s) = \frac{1}{2} (u_i(s) - \hat{u}_i(s))^T K_i (u_i(s) - \hat{u}_i(s)) \quad (4)$$

subject to the contact constraints, i.e., each tube must remain inside its outer neighbor.

B. Formulation as Vector Space Optimization

The optimization in the previous section can be converted to a vector space optimization by discretizing the arclength s and all the functions of s . First, let vector u and vector p denote the collection of discretized $u_i(s)$ and $p_i(s)$ for all $i = 1, \dots, n$, i.e.,

$$u = [u_1^T \ u_2^T \ \dots]^T \in \mathbb{R}^{3N} \quad (5)$$

$$p = [p_1^T \ p_2^T \ \dots]^T \in \mathbb{R}^{3N} \quad (6)$$

where

$$u_i = [u_i(s_{i1})^T \ u_i(s_{i2})^T \ \dots]^T \in \mathbb{R}^{3N_i} \quad (7)$$

$$p_i = [p_i(s_{i1})^T \ p_i(s_{i2})^T \ \dots]^T \in \mathbb{R}^{3N_i}. \quad (8)$$

Here, $\{s_{ij}\}_{j=1, \dots, N_i}$ are all the discretized points on tube i and N_i is the number of the points. N is the sum of N_i over all tubes, i.e., $N = \sum_{i=1}^n N_i$. Then, by (1) and (2), p is a function of u , i.e.,

$$p = F(u). \quad (9)$$

The contact constraint can also be expressed as a function of the vector p . For now, let us just write it by

$$G(p) \leq 0. \quad (10)$$

The objective in (3) is also rewritten with the vector u of the form

$$J = \frac{1}{2} (u - \hat{u})^T K (u - \hat{u}) \quad (11)$$

where $\hat{u} \in \mathbb{R}^{3N}$ is the discretized pre-curvature vectorized from $\{\hat{u}_i(s)\}_{i=1, \dots, n}$ in the same way as u , and $K \in \mathbb{R}^{3N \times 3N}$ is a diagonal matrix whose i -th diagonal component is the bending or torsional stiffness associated with i -th component of the curvature vector u . For example, the first and the second diagonal components of K are $k_{1,xy}$ and the third component is $k_{1,z}$.

Despite the convex objective function, this problem is not convex because the contact constraint is non-convex. By assuming small clearances and, accordingly, small differences in the tube curvatures from the solution of the zero-clearance model introduced at the beginning of Section II, the optimization reduces to a convex problem by linearizing (9) around the solution of the zero-clearance model.

Let $(u_i^*(s), R_i^*(s), p^*(s))$ denote the solution of the zero-clearance model, where $p^*(s)$ is not indexed with i as the centerlines are identical between tubes. Defining $\Delta u \in \mathbb{R}^{3N}$ and $\Delta p \in \mathbb{R}^{3N}$ as the differences in the curvatures and the centerlines from $u_i^*(s)$ and $p^*(s)$, the objective (11) becomes

$$\min_{\Delta u} \frac{1}{2} \Delta u^T K \Delta u + g^T \Delta u \quad (12)$$

where g is defined by

$$g = K(u^* - \hat{u}). \quad (13)$$

Here again, $u^* \in \mathbb{R}^{3N}$ is vectorized from $u_i^*(s)_{i=1, \dots, n}$ in the same way with u and \hat{u} .

Now let us focus on the contact constraint. Consider the cross section of the robot at $p_i(s)$ as shown in Figure 2. The

cross section intersects with $p_{i+1}(s + \epsilon)$, not $p_{i+1}(s)$, since integrating along the different centerlines results in different arc lengths on the cross section. The quantity ϵ is this arc length difference. While the cross section of the inner tube in Figure 2(b) is not a circle but an ellipsoid, let's assume it is a circle based on the small clearance assumption. Then the constraint can be written as

$$\|p_1(s) - p_2(s + \epsilon)\| \leq c_i \quad (14)$$

where the clearance $c_i (i = 1, \dots, n)$ is given by

$$c_i = r_{i,\text{in}} - r_{i+1,\text{out}}. \quad (15)$$

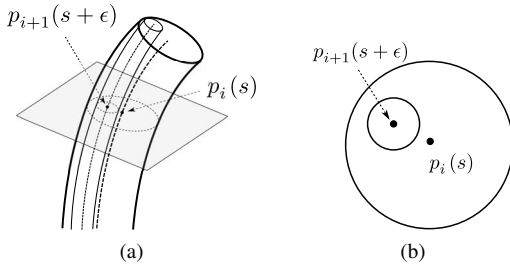


Fig. 2. Intersection of inner tube with cross section of outer tube. (a) Centerlines. (b) Plane of cross section.

Assuming small $\Delta p_1(s)$, $\Delta p_2(s)$ and ϵ , the first-order approximation of $p_1(s) - p_2(s + \epsilon)$ is given by

$$p_1(s) - p_2(s + \epsilon) \approx \Delta p_1(s) - \Delta p_2(s) - \epsilon \dot{p}^*(s). \quad (16)$$

Since (16) is a vector on the cross sectional plane, the projection of this vector onto the plane is the vector itself:

$$\Delta p_1(s) - \Delta p_2(s) - \epsilon \dot{p}(s) = P(s)(\Delta p_1(s) - \Delta p_2(s)) \quad (17)$$

where the projection matrix is approximated with $\dot{p}^*(s)$, i.e.,

$$P(s) \approx I_{3 \times 3} - \dot{p}^*(s)\dot{p}^*(s)^T \quad (18)$$

and $P(s)\dot{p}(s)$ vanishes since $\dot{p}(s)$ is the null vector of $P(s)$. Finally, the contact constraint reduces to

$$(\Delta p_1(s) - \Delta p_2(s))^T P(s)(\Delta p_1(s) - \Delta p_2(s)) \leq c_i^2. \quad (19)$$

This can be now expressed with the vector p of the form

$$\frac{1}{2} \Delta p^T S_{ij}^T P_{ij} S_{ij} \Delta p - q_{ij} \leq 0 \quad (20)$$

for all $i = 1, \dots, n-1$, $j = 1, \dots, N_i$. Here, the squared clearance q_{ij} is defined by

$$q_{ij} = \frac{1}{2} (r_{i,\text{in}} - r_{i+1,\text{out}})^2 \quad (21)$$

where $r_{i,\text{in}}$ and $r_{i,\text{out}}$ are the inner and outer radii of tube i , respectively. $S_{ij} \in \mathbb{R}^{3 \times 3N}$ is a selection to pick $\Delta p_i(s_{ij})$ and $-\Delta p_{i+1}(s_{ij})$ from Δp such that

$$S_{ij} \Delta p = \Delta p_i(s_{ij}) - \Delta p_{i+1}(s_{ij}), \quad (22)$$

and $P_{ij} \in \mathbb{R}^{3 \times 3}$ is a projection matrix given by

$$P_{ij} = I_{3 \times 3} - \dot{p}^*(s_{ij})\dot{p}^*(s_{ij})^T. \quad (23)$$

By the linearization, Δp is linear in Δu of the form

$$\Delta p = \Phi \Delta u \quad (24)$$

where Φ is given by

$$\Phi = \begin{bmatrix} \Phi_1 & & 0 \\ & \Phi_2 & \\ 0 & & \ddots \end{bmatrix} \in \mathbb{R}^{3N \times 3N} \quad (25)$$

where Φ_i is a $3N_i \times 3N_i$ lower triangular matrix whose (j_1, j_2) -th 3×3 block $\Phi_i(j_1, j_2)$ is given by

$$\Phi_i(j_1, j_2) = \begin{cases} [p(s_{ij_2}) - p(s_{ij_1})] R_i(s_{ij_2}) & \text{if } j_1 > j_2 \\ 0_{3 \times 3} & \text{otherwise} \end{cases} \quad (26)$$

Finally, the constraint (27) can be expressed as a convex constraint w.r.t. Δu :

$$\frac{1}{2} \Delta u^T X_{ij}^T X_{ij} \Delta u - q_i \leq 0 \quad (27)$$

where $X_{ij} = P_{ij} S_{ij} \Phi$.

Now the problem consists of the convex objective function and a set of convex constraints. This is computationally difficult to solve, however, owing to the high dimensionality of Δu and the large number of nonlinear constraints. For example, a standard iterative optimization involves gradient descent and projection onto the set of the violated constraints, which is costly in a high dimensional space with many nonlinear constraints. For this reason, we recast the problem as its dual [14] to reduce dimensionality and produce linear constraints.

C. Dual Problem Formulation

The dual problem involves optimizing over Lagrangian multipliers associated with the constraints of the original problem. The dimensionality of the dual problem is thus equal to the number of constraints in the original problem. The dual problem is a maximization and its objective function is always concave by nature and the constraints are simple and linear since the multipliers are nonnegative. Furthermore it has been shown that the dual problem attains the global solution of the original problem if the original problem was convex [14].

Following the formulations in [14], the dual problem of our problem is given as the following maximization:

$$\max_{\lambda} \left\{ J_{\lambda} = \frac{1}{2} g^T Q(\lambda)^{-1} g - q^T \lambda \right\} \quad (28)$$

subject to

$$\lambda_k \geq 0 \text{ for } k = 1, \dots, M \quad (29)$$

where $\lambda = [\lambda_1 \ \lambda_2 \ \dots]^T$ is a M -dimensional vector and M is the number of constraints, i.e., $M = \sum_{i=1}^{n-1} N_i$. $Q(\lambda)$ is defined as

$$Q(\lambda) = K + \sum_{k=1}^M \lambda_k X_k^T X_k \quad (30)$$

where X_k is renumbered with the index k from X_{ij} . The gradient of J_λ is then analytically given by

$$\frac{\partial J_\lambda}{\partial \lambda_k} = \frac{1}{2} g^T Q^{-1} X_k^T X_k Q^{-1} g - q_k. \quad (31)$$

Again, q_k is renumbered from q_{ij} . The relation between λ and Δu is then given by

$$\Delta u = Q(\lambda)^{-1} g. \quad (32)$$

For the efficient computation of J_λ and its gradient, one can compute Δu first from (32) since Q^{-1} always comes with g . This can be efficiently computed by solving the linear equation $Q\Delta u = g$ for given Q and g .

Gradient ascent with constraint projection works nicely with this problem thanks to the simple and linear constraints (29). The projection of λ onto the violated constraints can be done simply by setting all $\lambda_k < 0$ to be $\lambda_k = 0$.

Physically, these multipliers are proportional to the contact forces concentrated at the corresponding points. The force, f_k , can be derived as

$$f_k = c_i \lambda_k \text{ for } k = 1, \dots, M \quad (33)$$

based on a virtual displacement and energy analysis. Here, c_i is the clearance of the associated tube pair. Note that, since we have discretized the arc length, the distributed contact force is computed as a set of concentrated forces over continuous discretized points.

D. Algorithm

The algorithm to solve the dual problem optimization is as follows. The initialization steps include:

- solving the zero-clearance model to compute $(u_i(s), R_i(s), p_i(s))_{i=1, \dots, n}$,
- constructing matrix K based on the stiffnesses of the tubes,
- computing g from (13) based on the solution of the zero-clearance model,
- computing $q_k (= q_{ij})$ using (21),
- computing $X_k^T X_k (= X_{ij}^T X_{ij})$ using (22), (23), (25), and (26),
- initializing λ .

The optimization loop is as follows:

- 1) Compute Q from (30) for given λ
- 2) Solve $Q\Delta u = g$ for Δu .
- 3) Compute J_λ and $\frac{\partial J_\lambda}{\partial \lambda}$ in (28) and (31) using $\Delta u = Q^{-1}g$ from 2).
- 4) Update λ by $\lambda \leftarrow \lambda + \delta \frac{\partial J_\lambda}{\partial \lambda}$ with a small positive δ .
- 5) For all k , set $\lambda_k = 0$ if $\lambda_k < 0$.
- 6) Check convergence and terminate the loop if converged.
- 7) Go back to 1).

Once converged, the latest Δu can be used to compute Δp by (24). The centerlines of the tubes can then be given by adding Δp to $p_i(s)_{i=1, \dots, n}$.

One can adjust the initial λ , the termination condition and the step size of each iteration. In the examples considered below, λ was initialized as $\lambda = [1, 1, \dots]^T$ and the step size

TABLE I
PARAMETERS OF TUBE PAIR.

	Tube 1	Tube 2	
	Section 1	Section 1	Section 2
Length (mm)	150	17	150
Curvature (mm^{-1})	1/150	0.0	1/150
Bending Stiffness	1	1	1
Torsional Stiffness	1/1.3	1/1.3	1/1.3

TABLE II
PARAMETERS OF 3-TUBE ROBOT.

	Tube 1	Tube 2		Tube 3	
	Section 1	Section 1	Section 2	Section 1	Section 2
Length (mm)	150	17	150	184	86.4
Curvature (mm^{-1})	1/265	0.0	1/265	0.0	1/55
Bending Stiffness	1	1	1	1	1
Torsional Stiffness	1/1.3	1/1.3	1/1.3	1/1.3	1/1.3

δ was adapted by decreasing it 2% whenever J_λ decreased from the previous iteration. The termination condition was that J_λ increases by less than 10^{-9} .

III. NUMERICAL EXPERIMENTS

This section presents a set of numerical experiments to understand how the clearance influences the robot kinematics and the contact force distribution. Two different designs of concentric tube robots are used here: i) balanced tube pair, ii) 3-tube robot, whose tube parameters are given in Table I and in Table II, respectively. The tube pair is used through Section III-A to III-E and the 3-tube robot is used only in Section III-F.

Notice that the analysis is independent of the tube diameters and depends only on the clearances. Also note that the units of the contact forces are mm^{-2} throughout this section, which is the force unit normalized by the unit of the stiffness. Thus, the stiffnesses are dimensionless as given in Table I and Table II.

The tubes in the tube pair and the 3-tube robot are illustrated in Figure 3. Note that the collars shown at the proximal ends of the tubes are required to mount the tubes in the drive system and have a length of 17mm. The constraints introduced by the collars are included in the analysis.

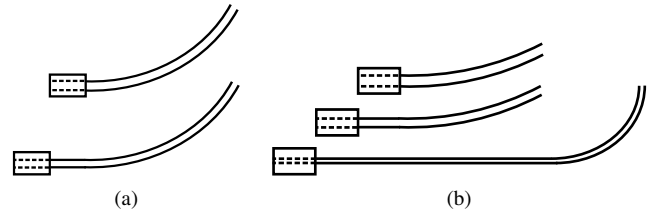


Fig. 3. Robot designs comprised of (a) a tube pair, and (b) three tubes.

A. Effect of Clearance on Tip Position

We first investigated the differences in the predictions of the robot tip position between the zero and nonzero clearance cases. Since it is assumed that a tool would be delivered

through the inner robot tube, its tip position is compared with that of the zero clearance model. Figure 4 plots tip position difference as a function of base rotation angle for five values of clearance as defined by (15). Tip position error is an increasing function of clearance and of base rotation angle up to 180° . A typical value of clearance in our robot designs is 0.1mm, which, over the 150mm robot length considered produces a maximum tip difference of 1.5mm.

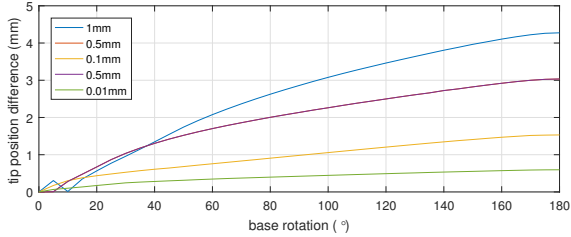


Fig. 4. Tip position difference for the inner tube between the zero clearance model for five values of clearance as a function of base rotation angle. The curves are plotted for 5° increments of the base rotation.

We note that the nonsmooth changes in difference for small base rotation angles, magnified in Figure 5, are due to the mounting collars. This effect is explained below in section III-E.

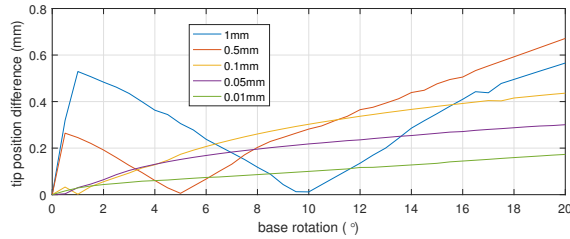


Fig. 5. Tip position error versus base rotation angle for small values of base rotation angle.

B. Effect of Clearance on Tip Tangent Direction

Figure 6 plots the difference in tangent direction as the angle between the zero and nonzero clearance tangent vectors for the inner tube. As before, the difference is an increasing function of clearance and base rotation angle. For a standard clearance value of 0.1mm, the maximum tangent angle difference is about 1 degree.

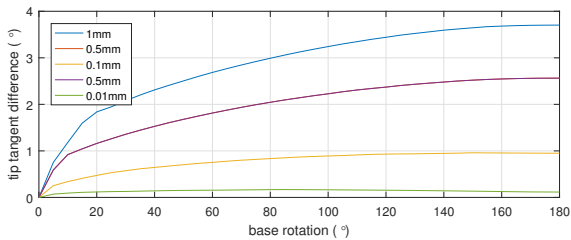


Fig. 6. Tip tangent direction angle difference comparing zero and nonzero clearance models for the inner tube as a function of base rotation angle.

C. Effect of Clearance on Contact Force Distribution

When the base of the tube pair is rotated by 180° , the zero-clearance model predicts a concentrated moment applied between the tubes at their tips. In reality, this concentrated moment is a combination of two forces applied at two different points that are close to each other. To see the effect of clearance on the magnitudes and the distances between the two forces comprising this moment, we plotted the forces as a function of arc length for $\theta_{2,b} = 180^\circ$ as shown in Figure 7. Note that, due to discretization, distributed forces are modeled as concentrated forces applied at the discretization points.

One can see there always exists a force at the tip for all nonzero clearances. There is also a set of forces with smaller magnitudes close the tip which result in a moment when combined with the tip force. As the clearance decreases, the forces increase in magnitude and approach each other so as to produce approximately the same net moment.

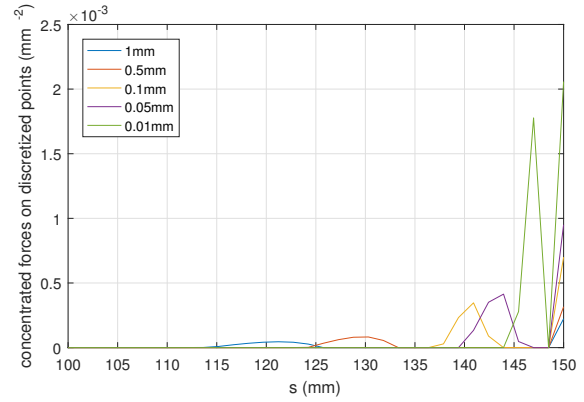


Fig. 7. Tip contact force distributions for five values of clearance. Note that forces are 3D and only magnitudes are plotted here.

D. Effect of Base Rotation Angle on Contact Force Distribution

The distribution of the contact forces and their magnitudes vary with the base rotation. It is obvious that there is no contact force when the base rotation of the tube pair is 0° . As base rotation angle increases 180° , the contact forces increase in magnitude and move towards the ends of the tubes. This is shown in Figure 8, where the contact forces are depicted as green circles with diameters indicating magnitude of force. The green circle at the tip obviously grows up as the base rotates. These force magnitudes are plotted versus arc length in Figure 9 for a superset of base rotation angles. The clearance is 0.1mm in both figures.

E. Effect of Clearance in Modeling the Effect of Collars and Straight Transmission Lengths

Figure 10(a) and (b) compare the centerlines of the inner (blue) and outer (red) tubes with and without the straight transmission length of the inner tube for a base rotation angle of 180° . The clearance in this figure is 3mm, which is

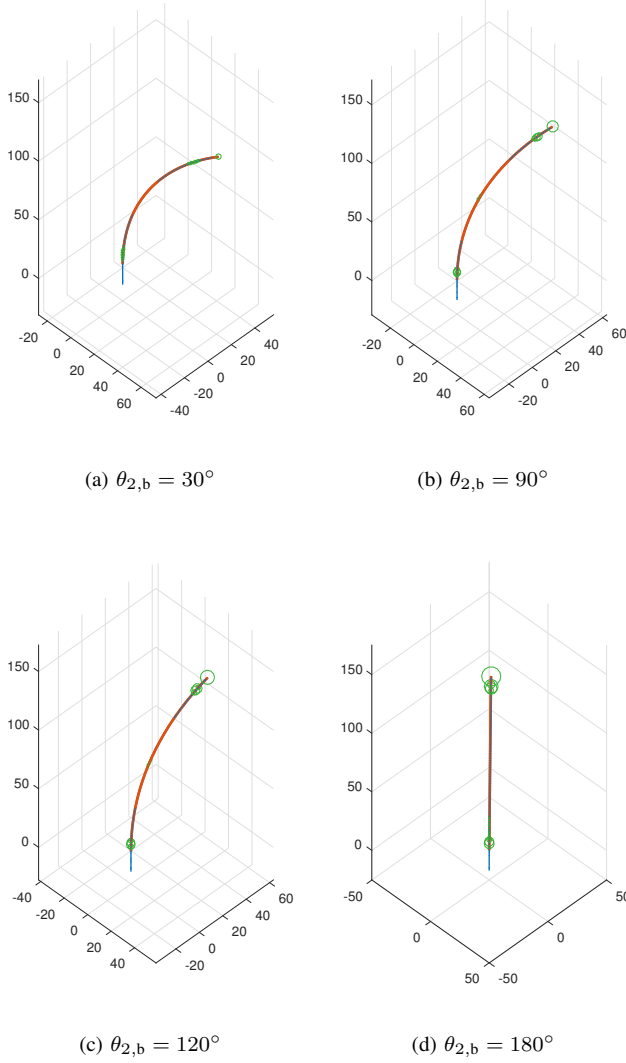


Fig. 8. Force distribution and magnitude as a function of base rotation angle when the clearance is 0.1mm. The contact forces are visualized with green circles whose sizes are proportional to the forces.

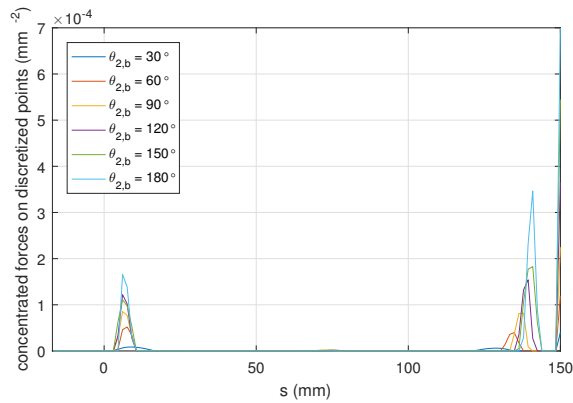


Fig. 9. Force distribution as a function of arc length for six values of base rotation angle when the clearance is 0.1mm.

selected for ease of visualization. For the case of no trans-

mission length, the centerlines of the tubes are symmetric as shown in Figure 10(a). In contrast, when the inner tube has a transmission length, the inner tube comes into the outer tube with a nonzero angle and the centerlines become dominated by the stiffer outer tube as shown in Figure 10(b).

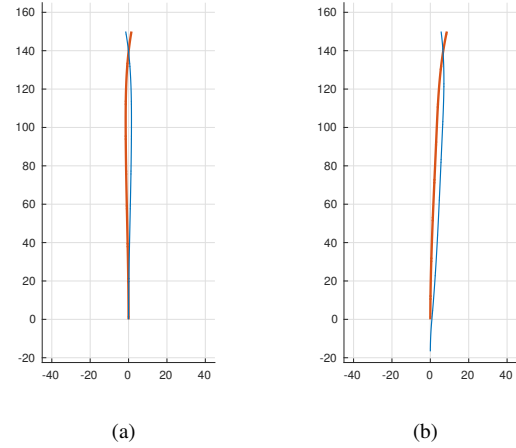


Fig. 10. Centerlines of inner (blue) and outer (red) tubes in presence of 3mm clearance with (a) no straight transmission lengths and (b) a 17mm straight transmission length of the inner tube. The tube centerlines in (b) are not symmetric due to the transmission length.

To show how this imbalance varies with the clearance, the mean of the tip positions of the tubes is compared with the tip position with zero clearance in Figure 11. It is observed that the mean point diverges from the tip position with zero clearance as the clearance increases. When the clearance is a standard value of 0.1mm, this mean point diverges 1.58mm away from the prediction of zero clearance model.

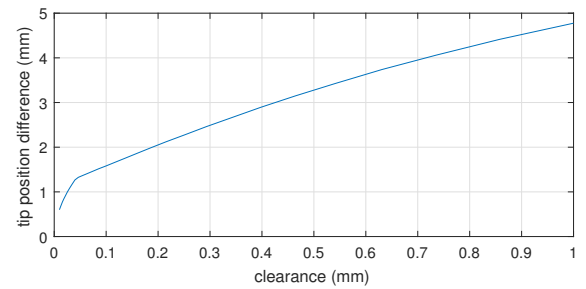


Fig. 11. Difference between mean tip position and tip position of zero-clearance model as a function of clearance.

It has been shown in Section III-A that the inner tube experiences a tip position difference that first increases, then decreases and then increases again for the small base rotations. This can be explained as follows. Initially, the tips of the both tubes diverge from the tip position predicted by zero clearance model. Up to this point, the tip positions of the inner and outer tubes are more or less symmetric w.r.t. the tip position predicted by zero clearance model. When the interaction between the tubes becomes significant, the outer starts pulling the inner tube towards itself and the tip of inner tube passes by through tip position predicted by

the zero clearance model. Then, as the base rotation goes to 180° , the tip position differences of both tubes increase as the overall shapes approach to the shapes in Figure 10(b).

F. Effect of Clearance on Tip Position of 3-Tube Robot

Assuming the base of the outermost tube is fixed, the configuration space of the 3-tube robot consists of the two rotations of tube 2 and tube 3 and one translation of tube 3. Since it is difficult to span the whole configuration space, we have picked a configuration where the base of tube 2 is rotated by 90° and the innermost tube is half-extended. In this configuration, all tubes experience torsion as well as bending. Figure 12 plots tip position difference between the zero and nonzero clearance cases for each tube as a function of tube clearance. For a standard clearance of 0.1mm, the tip position difference between two cases is 3.08mm.

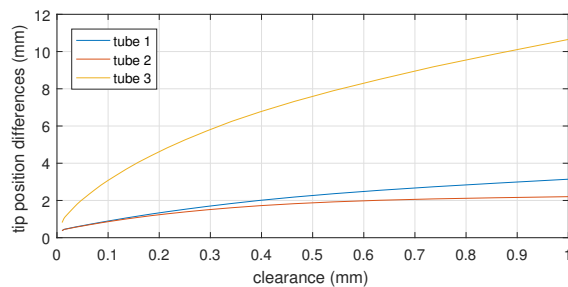


Fig. 12. Tube tip position error as a function of clearance.

IV. CONCLUSION

While the zero clearance assumption in the kinematics of concentric tube robots has been considered as a reasonable assumption, no prior efforts have been made to test this assumption. The analysis provided in this paper indicates that, while formulation of the finite clearance problem is challenging, it can be solved efficiently. Furthermore, while our primary goal in modeling clearance is as a step toward modeling friction, it has been shown that a frictionless clearance model predicts tip positions that can differ by several millimeters from the predictions of the zero-clearance model.

REFERENCES

- [1] N. V. Vasilyev, P. E. Dupont, and P. J. Del Nido, "Robotics and imaging in congenital heart surgery," *Future cardiology*, vol. 8, no. 2, pp. 285–296, 2012.
- [2] A. H. Gosline, N. V. Vasilyev, E. J. Butler, C. Folk, A. Cohen, R. Chen, N. Lang, P. J. Del Nido, and P. E. Dupont, "Percutaneous intracardiac beating-heart surgery using metal MEMS tissue approximation tools," *The International journal of robotics research*, vol. 31, no. 9, pp. 1081–1093, 2012.
- [3] C. Kim, A. Ataollahi, I. Berra, and P. Dupont, "Cardioscopic imaging to guide manual and robotic surgery inside the beating heart," *Hamlyn Symposium on Medical Robotics*, pp. 15–16, 2015.
- [4] N. V. Vasilyev, A. Gosline, A. Veeramani, M. Wu, G. Schmitz, R. Chen, V. Arabagi, P. J. del Nido, and P. E. Dupont, "Tissue removal inside the beating heart using a robotically delivered metal MEMS tool," *Int. J. Robotics Research*, vol. 34, no. 2, pp. 236–247, 2015.
- [5] J. Burgner, D. C. Rucker, H. B. Gilbert, P. J. Swaney, P. T. Russell, K. D. Weaver, and R. J. Webster III, "A telerobotic system for transnasal surgery," *IEEE/ASME Trans. Mechatronics*, vol. 19, no. 3, pp. 996–1006, 2014.
- [6] T. Anor, J. R. Madsen, and P. Dupont, "Algorithms for design of continuum robots using the concentric tubes approach: a neurosurgical example," in *Robotics and Automation (ICRA), 2011 IEEE International Conference on*. IEEE, 2011, pp. 667–673.
- [7] L. A. Lyons, R. J. Webster III, and R. Alterovitz, "Motion planning for active cannulas," *IEEE/RSJ Int. Conf. Intelligent Robots and Systems*, pp. 801–806, 2009.
- [8] L. Lyons, R. W. III, and R. Alterovitz, "Planning active cannula configurations through tubular anatomy," *IEEE Int. Conf. Robotics and Automation*, pp. 2082–2087, 2010.
- [9] L. G. Torres, R. J. Webster III, and R. Alterovitz, "Task-oriented design of concentric tube robots using mechanics-based models," *IEEE/RSJ Int. Conf. Intelligent Robots and Systems*, 2012.
- [10] P. E. Dupont, J. Lock, B. Itkowitz, and E. Butler, "Design and control of concentric tube robots," *IEEE Trans. Robotics*, vol. 26, no. 2, pp. 209–225, 2010.
- [11] D. C. Rucker, B. A. Jones, and R. J. Webster III, "A geometrically exact model for externally-loaded concentric-tube continuum robots," *IEEE Trans. Robotics*, vol. 26, no. 5, pp. 769–780, 2010.
- [12] D. C. Rucker, R. J. Webster, G. S. Chirikjian, and N. J. Cowan, "Equilibrium conformations of concentric-tube continuum robots," *The International Journal of Robotics Research*, vol. 29, no. 10, pp. 1263–1280, 2010.
- [13] J. Ha, F. C. Park, and P. E. Dupont, "Elastic stability of concentric tube robots subject to external loads," *Biomedical Engineering, IEEE Transactions on*, 2015.
- [14] S. Boyd and L. Vandenberghe, *Convex optimization*. Cambridge university press, 2004.